THE JOURNAL OF BIOLOGICAL CHEMISTRY VOL. 280, NO. 39, pp. 33652–33659, September 30, 2005

Ultrafast and Low Barrier Motions in the Photoreactions of the Green Fluorescent Protein*

Received for publication, May 18, 2005, and in revised form, June 29, 2005 Published, JBC Papers in Press, July 20, 2005, DOI 10.1074/jbc.M505473200

Jasper J. van Thor[‡1], **Georgi Y. Georgiev**[§], **Michael Towrie**[¶], **and J. Timothy Sage**[§]

From the [‡]*Laboratory of Molecular Biophysics, University of Oxford, Rex Richards Building, South Parks Road, Oxford OX1 3QU, United Kingdom,* [§]*The Department of Physics and Center for Interdisciplinary Research on Complex Systems, Northeastern University, Boston, Massachusetts 02115, and the* [¶]*Central Laser Facility, Council for the Central Laboratory of the Research Councils, Rutherford Appleton Laboratory, Chilton, Didcot, Oxfordshire OX11 0QX, United Kingdom*

Green fluorescent protein (GFP) fluoresces efficiently under blue excitation despite major electrostatic rearrangements resulting from photoionization of the chromophore and neutralization of Glu-222. A competing phototransformation process, which ionizes the chromophore and decarboxylates Glu-222, mimics the electrostatic and structural changes in the fluorescence photocycle. Structural and spectroscopic analysis of the cryogenically stabilized photoproduct at 100 K and a structurally annealed intermediate of the phototransformed protein at 170 K reveals distinct structural relaxations involving protein, chromophore, solvent, and photogenerated CO_2. Strong structural changes of the 100 K photoproduct after decarboxylation appear exclusively within 15 Å of the chromophore and include the electrostatically driven perturbations of Gln-69, Cys-70, and water molecules in an H-bonding network connecting the chromophore. X-ray crystallography to 1.85 Å resolution and static and picosecond time-resolved IR spectroscopy identify structural mechanisms common to phototransformation and to the fluorescence photocycle. In particular, the appearance of a 1697 cm^{-1} (+) difference band in both photocycle and phototransformation intermediates is a spectroscopic signature for the structural perturbation of Gln-69. This is taken as evidence for an electrostatically driven dynamic response that is common to both photoreaction pathways. The interactions between the chromophore and the perturbed residues and solvent are decreased or removed in the T203H single and T203H/Q69L double mutants, resulting in a strong reduction of the fluorescence quantum yield. This suggests that the electrostatic response to the transient formation of a buried charge in the wild type is important for the bright fluorescence.

Green fluorescent protein (GFP)[2] (1, 2) from *Aequorea victoria* is highly fluorescent with 400 nm excitation, despite major electrostatic rearrangements resulting from rapid charge transfer to the excited chromophore (3). Rapid excited state proton transfer (ESPT) (4–6) follows excitation of the neutral, phenolic chromophore, and the resulting excited phenolate state I* exhibits high quantum efficiency red-shifted emission at 508 nm, with a 3.0-ns lifetime (3). The mechanism by which the protein environment suppresses non-radiative processes remains unexplained. Proposals for the ESPT pathway include a hydrogen bonding network connecting the chromophore phenolic oxygen to Glu-222 via a water molecule and Ser-205 (7–9). Recently, the possibility of a proton transfer pathway including Glu-222, Asp-82, and Glu-5 was put forward (10). The transient infrared absorption reportedly developing at 1706 cm^{-1} with excitation of GFP in D_2O (9) could not distinguish between these proposals. However, experimental evidence for the identity of the proton acceptor has recently been provided from comparison with the E222D mutant (11).

Low quantum yield electron transfer from Glu-222 to the photoexcited chromophore triggers decarboxylation of the buried carboxyl group (12). This irreversible phototransformation process competes with ESPT that initiates the dominant fluorescence photocycle. The buried carboxylate of Glu-222 stabilizes the protonated chromophore via electrostatic repulsion (13). Neutralization of Glu-222 by light-induced decarboxylation therefore leads to chromophore ionization in equilibrium at pH 8.0 (12). Fig. 1 shows a simplified reaction scheme depicting the major charge redistributions for both the high quantum yield, reversible fluorescence photocycle, and the low quantum yield, irreversible, phototransformation pathway. The protein must relax to accommodate the electrostatic stress generated by chromophore ionization and neutralization of Glu-222, either in the phototransformed protein or following the ESPT reaction in the fluorescence photocycle. In the phototransformation pathway, we refer to the initial "dark" structure with a neutral chromophore (λ_{max} = 400 nm) as GFP_A, the initial "lumi" state produced by illumination at 100 K (λ_{max} = 497 nm) as GFP_L, the "meta" intermediate generated by thermal annealing of GFP_L as GFP_M, and the final, fully relaxed photoproduct previously characterized at 300 K (12) as GFP_R.

We describe structural events that follow charge transfer to the chromophore at cryogenic temperatures well below the protein dynamical transition (14), or on picosecond timescales at ambient temperature. We find the interior of the rigid β-barrel (13) to be significantly more fluid than the active site of previously characterized photoactive proteins (15–17), supporting the proposed (18) existence of protein conformational dynamics far below the solvent glass transition near 200 K. We conclude that rapid, low barrier structural dynamics stabilize the locally created buried charge and account for the bright fluorescence of GFP.

MATERIALS AND METHODS

Crystallization and Phototransformation—Wild type GFP was expressed and purified essentially according to a previous study (13). Crystals were grown at 4 °C in 100 mM Tris/HCl, 50 mM $MgCl_2$, and 15% polyethylene glycol 3350, pH 7.8, and cryo-protected using 20% glyc-

* This work is supported by grants from The Royal Society (University Research Fellowship to J. J. v. T.) and by National Institutes of Health and National Science Foundation Grants GM-52002 and PHY-0240955 (to J. T. S.). The costs of publication of this article were defrayed in part by the payment of page charges. This article must therefore be hereby marked "*advertisement*" in accordance with 18 U.S.C. Section 1734 solely to indicate this fact.

The atomic coordinates and structure factors (codes 1W7S, 1W7SSF, 1W7T, 1W7TSF, 1W7U, and 1W7USF) have been deposited in the Protein Data Bank, Research Collaboratory for Structural Bioinformatics, Rutgers University, New Brunswick, NJ (http://www.rcsb.org/).

[1] To whom correspondence should be addressed. Tel.: 44-(0)1865-285352; Fax: 44-(0)1865-275182; E-mail: jasper@biop.ox.ac.uk.

[2] The abbreviations used are: GFP, green fluorescent protein; ESPT, excited state proton transfer; GFP_L, lumi photoproduct state of GFP; GFP_M, metastable intermediate of GFP; GFP_R, relaxed photoproduct of GFP.

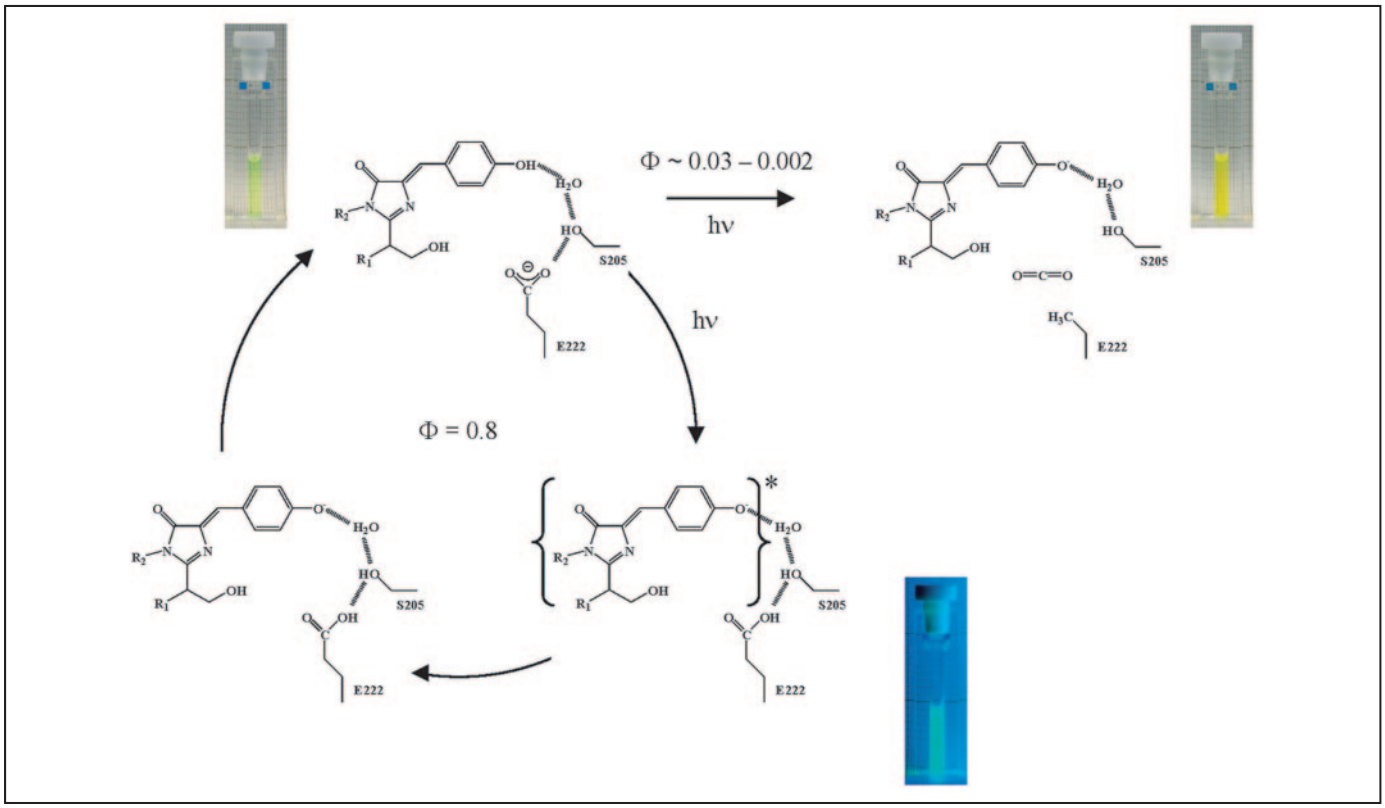

FIGURE 1. **Simplified reaction scheme for the fluorescence photocycle and phototransformation reaction pathways emphasizing charge redistribution.** Light-induced reactions are indicated with "*hν*," the electronically excited state is indicated between brackets, including the *asterisks*, quantum yields are given as "Φ," and the thermal and radiative reactions are indicated by *unmarked arrows*. The quantum yield for the phototransformation reaction is wavelength-dependent (12). Kinetics are not given for the simplified scheme, which does not take into account all known intermediates and associated changes but emphasizes the similarity between the charge redistribution on the chromophore and the buried carboxyl group in the reactant and product states. Photographs of *green* and *yellow* solutions of GFP and the decarboxylated photoproduct, respectively, show transmission, whereas the photograph of the fluorescent state shows *green* emission with UV excitation.

erol, 100 mM Tris/HCl, 50 mM $MgCl_2$, and 15% polyethylene glycol 3350, pH 7.8. For the initial studies, GFP_A crystals with various dimensions were exposed to an increasing dosage of short-wavelength UV radiation, and x-ray diffraction data were collected, using an in-house rotating anode source, to 2.4-Å resolution. The progressive disappearance of electron density of the γ-carboxylate of Glu-222 was used as an indicator for phototransformation. For these initial studies structures were not fully refined, and crude phases obtained from molecular replacement, rigid body and limited restrained refinements were sufficient to estimate the electron density changes at Glu-222. The progressive appearance of additional difference features in the unrefined $F_L - F_A$ map at 2.4-Å resolution resembled those later determined at higher resolution (Fig. 2, *A–C*), indicating the accumulation of the lumi state GFP_L. Off-line microspectrophotometric measurements were done at 100 K to monitor the phototransformation as well as fluorescence and absorption measurements of dissolved crystals after illumination. Together, these tests indicated that with illumination normal to the crystallographic *b*-axis of a crystal with a typical cross-section of 30 μm × 30 μm, complete phototransformation and trapping of a first intermediate at 100 K was achieved by illumination with a short-wavelength UV source (Universal UV lamp (Type TL-900) CAMAG, Muttenz, Switzerland, $\lambda_{max} = 254$ nm), with a dose of 0.1 mJ cm^{-2} s^{-1} for 75 min while continuously rotating the crystal. The extinction at 254 nm for half the path length (15 μm) was calculated to be 0.7, using an estimated extinction coefficient of 20 mM^{-1} cm^{-1}.

X-ray Data Collection—A crystal with dimensions of 30 μm × 30 μm × 200 μm was flash-frozen in liquid nitrogen, mounted in a CryoLoop, and maintained at 100 K using an Oxford Instruments Cryojet operating at a flow rate of 6.0 liters/min. X-ray diffraction data were collected at beamline 14.2 at the Synchrotron Radiation Source, Daresbury, UK. The wavelength was 0.978 Å, an Area Detector Systems Corporation Q4R charge-coupled device detector was used, and the front slits were set to 100 μm × 200 μm. Before phototransformation, a first GFP_A dataset was recorded to 1.85-Å resolution (TABLE ONE). After phototransformation, the crystal was translated ~50 μm, and a new dataset was recorded for the early photoproduct GFP_L (TABLE ONE). Subsequently, the crystal was heated to 170 K with a ramp rate of 6 K/min and kept at this temperature for 15 min for structural annealing. The crystal was re-cooled to 100 K with a ramp rate of 6 K/min, translated by 50 μm, and the final GFP_M dataset was recorded (TABLE ONE). The crystal volume exposed to x-ray radiation for more than a single set of images was minimized by the translation, and the beam overlap between datasets was estimated to be <50 μm. The data collection and integration statistics were very similar for all three datasets (TABLE ONE), indicating that no appreciable radiation damage had occurred.

Structure Solution and Refinement—The intensities were integrated with MOSFLM (19) and scaled with SCALA (20). 5% of the reflections were selected for R_{free} calculations, and the same set was selected in the photo-product (F_L) and high temperature-annealed (F_M) data-sets. Molecular replacement was performed with MOLREP (20), using 1HCJ as a search model. Building was performed using O, and the structures were refined with REFMAC (20) and ARP/WARP (21) without using non-crystallographic symmetry restraints. Refinement of chromophore atoms in the phenolic and imidazolinone rings were done with increased planar restraints. The intensities of the 100 K photoproduct (I_L) and the 170 K annealed (I_M) diffraction experiments were scaled to the first, dark (I_A) dataset using SCALEIT (20), with refinement of scale

TABLE ONE

Data-collection and refinement statistics

Structure	GFP_A	GFP_L	GFP_M
Space group	C2	C2	C2
Unit cell (a, b, c)/Å, (α, β, γ)/°	154.97 52.73 141.63 90.00 120.01 90.00	155.31 52.82 141.94 90.00 120.07 90.00	154.82 52.66 141.88 90.00 120.27 90.00
Resolution range[a]/Å	37.53–1.85/1.95–1.85	36.76–1.85/1.95–1.85	33.15–1.85/1.95–1.85
Total/unique reflections	388728/85082	470013/85530	496456/85637
Completeness[a]/%	97.5 / 86.0	97.6/86.6	97.3/84.0
Multiplicity	3.0 / 2.2	3.7/ 2.7	3.9/2.9
$I/\sigma(I)$[a]	6.7/4.2	5.5/2.9	5.7/2.8
R_{sym}[a,b]/%	0.066 / 0.172	0.084 / 0.248	0.080 / 0.262
Model refinement statistics			
Protein chains per asymmetric unit	4	4	4
Protein atoms/solvent atoms (per asymmetric unit)	7314/922	7315/922	7303/930
R_{work}/R_{free} value[c]	0.176 / 0.215	0.179 / 0.218	0.178/0.225
Mean B-value/Å^2			
All atoms	18.9	20.0	22.2
Protein atoms (chain A–D)	16.0 18.9 16.9 18.4	17.1 20.0 18.0 19.4	19.3 22.3 20.6 21.9
Water atoms	29.7	31.2	31.6
Bond length deviation root mean square delta/Å	0.012	0.013	0.013
Bond angles deviation root mean square delta/°	1.48	1.51	1.52
Restrained B-values (bond/angle)/Å^2	0.73/1.45	0.77/1.54	0.82/1.64

[a] Values for the highest resolution shell are given after the slash.
[b] $R_{sym} = \Sigma|I - \langle I\rangle|\Sigma I$.
[c] $R_{work} = \Sigma||F_{obs}| - k|F_{calc}||/\Sigma|F_{obs}|$. 5% of the reflections for the calculation of R_{free} were randomly chosen in the GFP_A dataset and copied to the GFP_L and GFP_M datasets.

factors and anisotropic B-factors. I_L and I_M were scaled to I_A with 82,131 and 82,242 common reflections, 1.001 and 1.006 scale factors, R-factors of 0.080 and 0.15, and error-weighted R-factors of 0.078 and 0.11, respectively. Normal probability analysis showed a value of δ(real)/δ(expected) = 1.3 and 1.4 for centric and acentric reflections for the scaling of I_L to I_A, δ(real)/δ(expected) = 1.9 and 2.0 for scaling of I_M to I_A, and δ(real)/δ(expected) = 1.2 and 1.4 for scaling of I_M to I_L. The fitted slopes of the normal probability plots were constant for all resolution bins and had near zero intercepts. The isomorphous differences were distributed normal in all resolutions bins for the scalings performed. $F_L - F_A$, $F_M - F_L$, and $F_M - F_A$ difference electron density maps were calculated using FFT (20), with rejection of a (high frequency Fourier term) outlier, and used to aid the model building of the photo-product and annealed structures. The final $F_L - F_A$ and $F_M - F_L$ difference maps shown in Figs. 2 and 3*C* were calculated using phases from the GFP_A and the GFP_L structures after complete refinement, respectively. For modeling water molecules in the GFP_L and thermally annealed GFP_M structures that are different from those in the GFP_A structure, the criterion applied was that convincing $2F_o - F_c$ density was present as well as density in $F_o - F_c$ omit maps.

With contouring of the $F_L - F_A$ difference map at an intensity of 3σ, rather than 5σ (Fig. 2, *A–C*), additional positive and negative difference electron density is revealed significantly further away from the chromophore, covering a large part of the volume of the protein and its hydration shell. At this contouring level, differences between the four chains become apparent, whereas the very strong signals (>5σ) are more similar in the four different chains

Mutagenesis—The T203H/Q69L double mutant was created starting from an expression construct for PA-GFP (T203H) (22), kindly provided by Jennifer Lippincott-Schwartz, using the QuikChange (Stratagene) protocol for the Q69L mutation using primer sequences CAGCTACGGCGTGCTGTGCTTCAGCCGC and GCGGCTGAAGCACAGCACGCCGTAGCTG.

Static Infrared Measurements—A cryo-loop containing either a hydrated GFP film equilibrated at 33% relative humidity or a GFP solution in 75% glycerol was mounted on an Fourier transform infrared microscope, and data were recorded at 2 cm^{-1} resolution with the sample temperature controlled by a cold nitrogen gas stream flowing at 5 liters/min. Either the 254 nm line of a mercury lamp or the 413 nm line of a krypton laser illuminated the sample until no further increases in the photogenerated CO_2 bands were observed. For room temperature measurements, solutions were mounted between calcium fluoride windows separated by a 15-μm spacer. IR difference spectra recorded with wild type GFP were identical to the GFPuv (F99H/M153T/V163A (23)) solution data presented in Fig. 3. GFPuv was used for most solution studies because of better solubility relative to wild type GFP.

Picosecond Time-resolved Infrared Measurements—Time-resolved IR measurements were recorded at the PIRATE facility at the Rutherford-Appleton Laboratory (24). The 400 nm second harmonic of a Ti:sapphire laser excited a 6–8 mM solution of GFPuv, prepared in either H_2O or D_2O, and loaded in a 6- to 12-μm path length infrared cell. Difference frequency mixing of the signal and idler of an optical parametric amplifier in a type I $AgGaS_2$ crystal generated a 100-nJ IR pulse with 200-fs pulse width centered at 1720 cm^{-1} (150 cm^{-1} full width at half-maximum), which was separated into probe and reference pulses. The IR probe pulse and 400 nm excitation pulse were focused into the sample to ~150-μm diameter spot size. The transmitted probe pulse was dispersed with 4-cm^{-1} resolution in a grating spectrograph, detected with a 64-element MCT array, and normalized pixel-by-pixel and pulse-by-pulse with respect to the similarly detected reference pulse. Reported spectra are differences between measurements of probe pulses recorded in the presence and absence of the excitation pulse, optically delayed by the given time with respect to the excitation pulse. The instrument response time was 400 fs. Raster scanning and periodic sample replacement avoided photodegradation, as confirmed by monitoring the visible absorption spectra.

RESULTS

Structure of the GFP_A Ground State—The space group of the crystals was C2, with four monomers in the asymmetric unit. Structure refine-

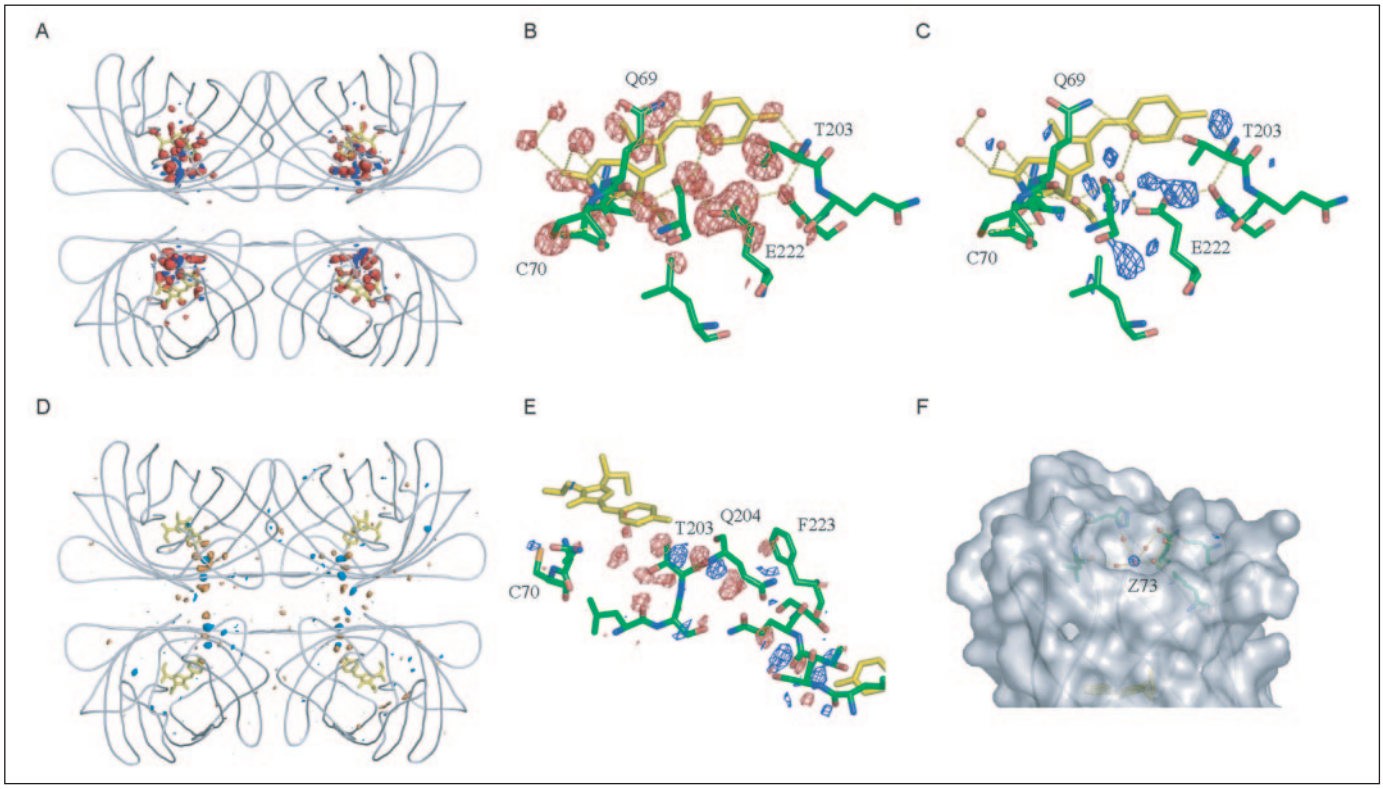

FIGURE 2. **Conformational changes at 100 K (*A–C*) and under annealing at 170 K (*D–F*).** *A*, $F_L - F_A$ electron density difference maps in the asymmetric unit contoured at 5σ (*red*) and -5σ (*blue*) reveal features exclusively present in a 15-Å diameter sphere containing the chromophore in each of the four chains. *B*, negative electron density map for chain A exclusively present at a contour level of -5σ. Strong negative features are found on the OH, O2, O3, $O_{\gamma 2}$ oxygen atoms as well as the N2, $C_{\alpha 2}$, $C_{\beta 2}$, and $C_{\delta 2}$ atoms of the chromophore. Additional negative electron density features are associated with Thr-203, Ser-205, Phe-64, Val-68, Cys-70, Gln-69, Leu-42, Leu-220, Ser-72, Gln-204, and the crystallographic waters Z78, Z80, Z81, Z111, Z220, Z223, and Z245. *C*, corresponding positive electron density map, with features associated with Thr-203, Val-224, Leu-42, Gln-204, Ser-72, and the solvent filled cavity. *D*, $F_M - F_L$ difference electron density map caused by structural annealing at 170 K contoured at 4σ (*orange*) and -4σ (*cyan*). *E*, detail of the $F_M - F_L$ difference map in chain A, showing movements of Thr-203 and Gln-204 to perturb Phe-223 in chain D. *F*, positive difference electron density centered on the cavity-bound crystallographic water molecule Z73 (of GFP_A). The isotropic temperature factors for this water, averaged over all four chains, are 13.2 Å^2, 13.4 Å^2, and 12.0 Å^2 in the GFP_A, GFP_L, and GFP_M structures, respectively, corresponding to an average root mean square displacement of 0.41 Å, 0.41 Å, and 0.39 Å.

ment and building showed differences between the four chains, and hence no NCS restraints were applied at any stage. The asymmetric unit contained two dimers that have an interface that is centered on Phe-223, similar to other dimer structures (12). In the chromophore region of the A structure, in particular with respect to the conformation of Glu-222 and Thr-203, the electron density supports a structure that is similar to the wild type crystal structure 1GFL solved at 1.9-Å resolution at pH 6.8 (13). In particular, the Glu-222 side chain is not in a rotamer conformation, but is best modeled and refined with the angles $\chi_1 = 62°$, $\chi_2 = 153°$, and $\chi_3 = -145°$, although the electron density indicates some disorder of the side chain (11). This conformation contrasts with the wild type structure solved at 2.13-Å resolution at pH 3.9, where Glu-222 was modeled with angles $\chi_1 = -29°$, $\chi_2 = -160°$, and $\chi_3 = -69°$ (1EMB (7)). Also, in our GFP_A structure, there is no indication of an alternative rotamer conformation of Thr-203, as modeled in the low pH structure (7).

X-ray Structure and IR Spectroscopy of the 100 K GFP_L Photoproduct—In contrast with cryogenically trapped intermediates of other photoactive proteins (15–17), unambiguous and strong structural changes at 100 K are evident from the unaveraged $F_L - F_A$ difference electron density map (Fig. 2, *A–C*). The normal distribution of isomorphous differences in all resolution bins, the correspondence between *R*-factors and error-weighted *R*-factors in the resolution ranges, the fall off of isomorphous differences with increasing resolution, and constant slope of the normal probability plots over all resolution bins all indicate the statistical relevance and low noise level of the strong electron density present in the difference Fourier map. Strong negative features in excess of 20σ cover the $O_{\epsilon 1}$, $O_{\epsilon 2}$, and C_δ atoms of Glu-222 in all four chains, resulting from the specific and complete light-induced decarboxylation of this residue in crystals of GFP. Net charge transfer from Glu-222 to the chromophore drives many additional conformational changes in the chromophore and its immediate environment, and difference density indicates greater active site disorder in GFP_L than in GFP_A (Fig. 2). The changes include perturbation of the Gln-69 side chain, which moves away from Thr-203 by hinging around the C_α atom. The Cys-70 side chain becomes more disordered, and the distance from the sulfur to the Val-68 carbonyl oxygen increases by 0.15 ± 0.01 Å in the refined coordinates, consistent with the $F_L - F_A$ difference density (Fig. 2).

Spectroscopic changes also reflect these substantial structural responses to chromophore ionization in both crystals and solutions. The pronounced shift of the visible absorption (Fig. 3*B*) and prominent spectral changes in the congested 1000–1800 cm^{-1} region of the $GFP_L - GFP_A$ IR difference spectrum (Fig. 3*A*) resemble those previously attributed to ionization of the chromophore (25). In particular, isotope substitutions and density functional theory calculations on a model compound for the GFP chromophore (26) suggest assignment of positive bands associated with vibrations of the phenol group (1497 and 1582 cm^{-1}), the imidazolinone ring (1537 cm^{-1}), and the bridging carbon (1615 cm^{-1}) of the anionic chromophore in the room temperature IR difference spectrum (11, 25).

We identify a new feature having positive and negative peaks at 1697 and 1691 cm^{-1} with a perturbation of the side chain C=O stretch of Gln-69, based on its characteristic frequency (27) and the absence of this feature in the phototransformed Q69L/T203H mutant (Fig. 4). We

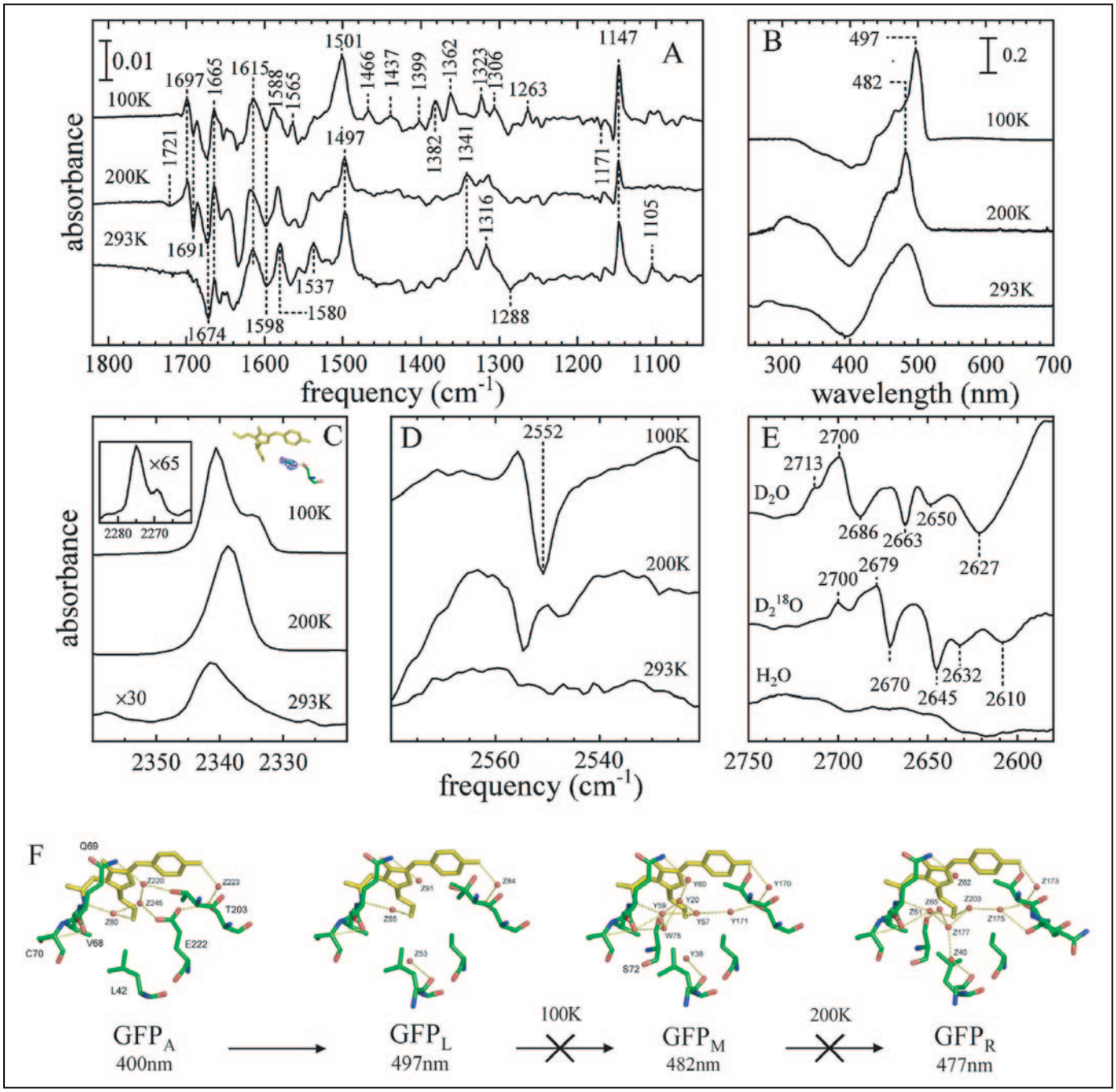

FIGURE 3. **Data in *A–E* characterize differences among the GFP_A, GFP_L, GFP_M, and GFP_R structures displayed in *F*.** Difference spectra recorded upon phototransformation of a hydrated film at 100 K, of a solution in 75% glycerol at 200 K, and of an aqueous solution at 293 K reflect $GFP_L - GFP_A$, $GFP_M - GFP_A$, and $GFP_R - GFP_A$ differences, respectively. The various spectral regions monitor chromophore and protein side-chain vibrations in the congested 1000–1800 cm^{-1} region (*A*), bleaching of the broad absorption band near 400 nm due to the neutral chromophore in the GFP_A state and the appearance of red-shifted bands due to the anionic chromophore in the GFP_L, GFP_M, and GFP_R states (*B*), vibrations of photogenerated CO_2 in the 2340 cm^{-1} region (*C*), reduced intensity of the Cys-70 S–H stretching vibration at 2552 cm^{-1} in the GFP_L and GFP_M states (*D*), and perturbation of weakly hydrogen-bonded internal water molecules near 2600 cm^{-1} in a D_2O-hydrated GFP film (*E*). *Insets* in *C* show the 2275 cm^{-1} region for $^{13}CO_2$ at 100 K and a strong positive feature in the $F_L - F_A$ difference map near Glu-222 in chain C. Spectra in *A*, *C*, *D*, and *E* are normalized to maintain constant CO_2 band area, except where indicated by explicit scale factors in *C*. *F*, coordinates for GFP_A (PDB 1W7S), GFP_L (PDB 1W7T), GFP_M (PDB 1W7U), and GFP_R (PDB 1HCJ).

found that the Q69L/T203H double mutant can readily be phototransformed, in contrast to the Q69L single mutant, for which the chromophore is ionized in equilibrium (28). Decreased absorbance of a 2552 cm^{-1} S–H stretching mode (Fig. 3*D*) is consistent with weakening of the Cys-70 S_γ–H . . . O Val-68 hydrogen bond in GFP_L. The appearance of multiple overlapping CO_2 bands (Fig. 3*C*) suggests significant disorder for the photogenerated CO_2. Together with the dominant negative contributions to the difference electron density, the additional disorder of the CO_2 molecule underscores the unexpected mobility of the chromophore environment at 100 K. Polarized IR data on oriented single crystals[3] supports the presence of the Cys-70 . . . Val-68 hydrogen bond and indicates a minimum of three CO_2 environments with distinct frequencies and orientations.

Negative signals corresponding to crystallographic waters in the chromophore vicinity also contribute prominently to the $F_L - F_A$ dif-

[3] G. Y. Georgiev, J. J. van Thor, and J. T. Sage, manuscript in preparation.

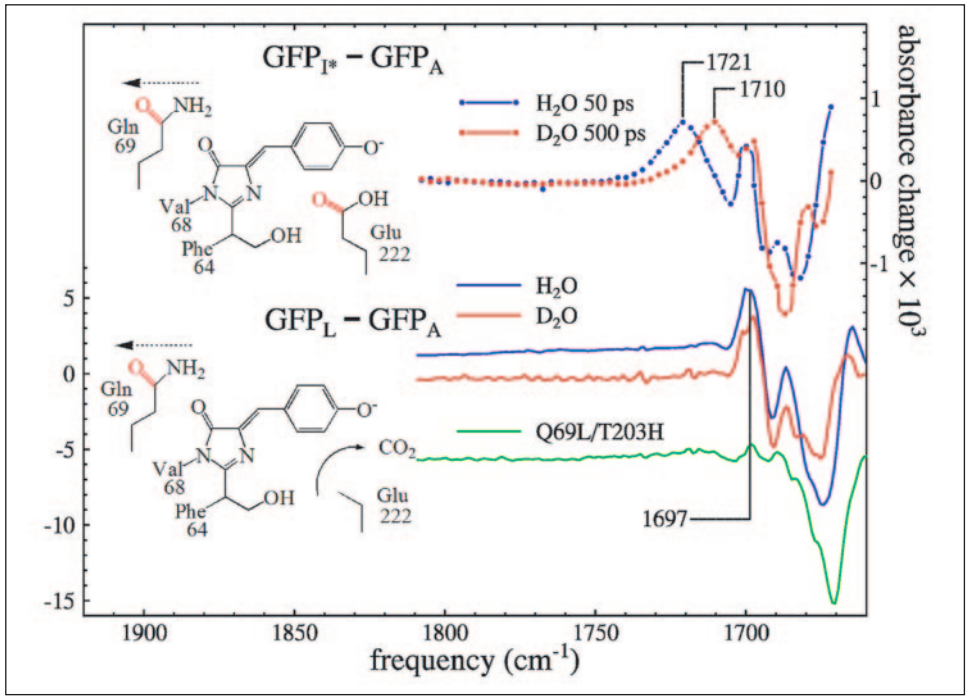

FIGURE 4. **Vibrational spectra probe common structural responses to electrostatic rearrangements in the fluorescence and phototransformation pathways.** GFP$_{I*}$ − GFP$_A$ IR difference spectra, recorded 50 ps after excitation of GFP$_A$ with a 400-nm excitation pulse, reveal a 1721-cm^{-1} band having a frequency and hydrogen isotope sensitivity consistent with the carbonyl stretch of a carboxylic acid that becomes protonated in the GFP$_{I*}$ state. A longer 500-ps delay time is chosen for the D$_2$O solution, to account for the kinetic isotope effect observed for deprotonation of the chromophore (3). The 1721 cm^{-1} band is absent in static GFP$_L$ − GFP$_A$ difference spectra recorded at 100 K, where phototransformation eliminates the Glu-222 proton acceptor, but the persistence of the 1697-cm^{-1} signal suggests a similar electrostatic stress, due to the creation of the anionic chromophore. The absence of the 1697-cm^{-1} feature in the phototransformation-induced IR difference signal of the Q69L/T203H mutant at 100 K supports assignment of this feature to Gln-69.

ference map, accompanied by weaker positive features. These include an incompletely hydrogen-bonded water cluster Z245, Z80, and Z220 (numbering for chain A of GFP$_A$), which initially hydrogen bonds to the side chains of Gln-69, Thr-203, and Glu-222, to the amide nitrogen of Val 68, and to $O_{\gamma 2}$ of the chromophore (Fig. 2), but undergoes significant restructuring to form a new stable H-bonded position in the fully relaxed GFP$_R$ photoproduct state (12). The D$_2$O-hydrated GFP$_L$ − GFP$_A$ IR difference spectrum (Fig. 3*E*) reveals signals in a frequency range characteristic for "dangling" O–D bonds. The dipoles of these weakly hydrogen-bonded waters can presumably reorient to stabilize the ionized chromophore more rapidly than in bulk solvent.

Solution measurements at 100 K confirmed that selected features of the GFP$_L$ − GFP$_A$ IR difference spectrum (Fig. 3) develop with identical kinetics, ruling out significant contributions from additional photochemical processes at this temperature. Moreover, identical IR spectral changes, including the appearance of CO$_2$ bands, resulted from illumination at either 254 or 413 nm. The latter measurement indicates the absence of significant heating effects, even with the order of magnitude reduction in the phototransformation quantum yield (12) at 413 nm. The total number of photons absorbed during phototransformation of our GFP crystal at 100 K is five orders of magnitude below that reported to enable migration of photolyzed CO in myoglobin at cryogenic temperature, where structural changes of the polypeptide are not observed in a 4σ difference map (29). Apparently, significant additional relaxation of GFP does not take place during the few picoseconds needed for the excited chromophore to cool. Bulk heating by the UV light source is discounted on the basis of calculations and experimental tests using a thermocouple device, as is heating from x-ray absorption (30).

X-ray Structure and IR Spectroscopy of the Thermally Annealed GFP$_M$ State—The structure evolves further in a GFP$_L$ crystal that is heated from 100 to 170 K, maintained at this temperature for 15 min, and re-cooled to 100 K. The resulting $F_M - F_L$ difference electron density map (Fig. 2*D*) reveals structural changes throughout the volume covering all the monomers, including the formation of a hydrogen-bonded cluster of new structural waters in the chromophore environment. A prominent series of positive and negative features reflects reorientation of the Thr-203 side chain, coupled to movements of the Gln-204 side chain and the Phe 223 side chain of the neighboring chain in the dimer (Fig. 2*E*). The new orientation, with Thr-203 within hydrogen bonding distance of the chromophore phenol oxygen, was previously observed in GFP$_R$ (12) as well as in the S65T mutant containing an anionic chromophore (31) and contrasts with the small degree of reorientation (estimated at 10% occupancy) in the GFP$_L$ structure.

Spectroscopic properties of the GFP$_M$ intermediate produced by phototransformation at 200 K (λ_{max} = 480 nm) are intermediate between those observed for the GFP$_L$ and GFP$_R$ states (Fig. 3, *A* and *B*). Relaxation of the chromophore environment following ionization is evident from the evolution of several features with heating to higher temperatures, in particular a phenolate mode at 1362 and 1341 cm^{-1} at 100 and 293 K, respectively (Fig. 3*A*). The 1300–1500 cm^{-1} region of the light-induced GFP$_M$ − GFP$_A$ difference spectrum recorded at 200 K resembles the GFP$_R$ − GFP$_A$ difference spectrum recorded at ambient temperature, rather than the GFP$_L$ − GFP$_A$ spectrum recorded at 100 K (Fig. 3*A*). However, the persistence of the 1697 cm^{-1} signal assigned to Gln-69 (Fig. 3*A*) and the Cys-70 S–H bleach (Fig. 3*D*) confirms the formation of a distinct intermediate state at 200 K. The IR spectral differences assigned to Gln-69 and to Cys-70 only disappear upon transition to the GFP$_R$ state at higher temperatures, where the protein conformation can fully relax to accommodate the molecular stress induced by phototransformation.

The H$_2$O/CO$_2$ cluster exhibits significant mobility in the chromophore cavity upon annealing. The CO$_2$ vibrational signals evolve over the 100–200 K temperature range, coalescing into a single band at 2338 cm^{-1} at 200 K (Fig. 3*C*). Although the $F_M - F_A$ difference map retains the positive feature associated with CO$_2$ in the $F_L - F_A$ map (Fig. 3*C*, *inset*), a new water molecule partially occupies this site in the GFP$_M$ structure, whereas no additional or new electron density can be attributed to the displaced CO$_2$ molecule (Fig. 3*F*). The progressive ordering of solvent in the active site (Fig. 3*F*) suggests that the GFP$_L$ → GFP$_M$ and GFP$_M$ → GFP$_R$ transitions are entropically unfavorable, and thus indicate that the overall pathway is enthalpically driven. Also, strong positive $F_M - F_L$ density for a well ordered surface-bound crystallographic water Z73 already present in GFP$_A$ and GFP$_L$ (Fig. 2*F*) indicates that

long range structural annealing enhances the ordering or occupancy of this hydration water.

Picosecond Transient IR Absorption Reveals a Common Structural Response in the Fluorescence and Phototransformation Pathways—The ESPT model for the fluorescence photocycle (7, 8) predicts an intermediate structure I* with an electrostatic environment resembling that following phototransformation, because the chromophore is ionized and the proposed Glu-222 terminal proton acceptor is neutralized. Indeed, time-resolved infrared difference absorption measurements on GFP 50 ps after 400 nm excitation of the neutral chromophore (Fig. 4) reveal a positive feature at 1721 cm^{-1}, in addition to the 1697 cm^{-1} Gln-69 signal. The 1721 cm^{-1} frequency, characteristic for C=O stretching of a strongly hydrogen-bonded neutral carboxylic acid (32), and its 11 cm^{-1} downshift with H/D exchange suggest Glu-222 as the terminal proton acceptor, because other acidic residues are exposed to solvent and are expected to be fully ionized in equilibrium at pH 8. This evidence is in agreement with a recent proposal (9, 11). Further corroboration results from transient infrared measurements on the E222D mutant (11). Both 1721 cm^{-1} and 1697 cm^{-1} bands are already observed 5 ps after excitation, signaling very rapid proton transfer to Glu-222 and ultrafast structural perturbation of Gln-69.

DISCUSSION

We have investigated the structural and spectroscopic changes that occur in the phototransformation pathway that is triggered by the light-induced decarboxylation of the buried glutamate 222 side chain. Phototransformation at low temperature produces a lumi photoproduct, GFP_L, that is characterized by strong structural changes relative to the ground state GFP_A, as determined by x-ray crystallography. Spectroscopic changes in the mid-infrared show that the GFP_L state is unrelaxed, and difference bands can be assigned to specific amino acid side chains on the basis of the x-ray structure, the polarization of infrared absorption of phototransformed crystals, and mutagenesis. In particular, the 1697 cm^{-1} is assigned to structural perturbation of Gln-69 and the 2552 cm^{-1} band to Cys-70. With subsequent heating, structural annealing of the GFP_L photoproduct produces the metastable intermediate GFP_M, which is characterized by specific solvent reorganization and protein motions. Picosecond time-resolved transient infrared measurements of the fluorescence cycle show that the structural response to optical excitation is similar to the response in the phototransformation reaction pathway.

The presence of the 1697 cm^{-1} Gln-69 band in the GFP_{I^*}, GFP_L, and GFP_M intermediates points to common structural mechanisms in the fluorescence and phototransformation pathways, and suggests that the structures reported here mimic intermediates in the fluorescence photocycle. This spectroscopic signature reflects the strong structural perturbation of Gln-69 that is evident in the $F_L - F_A$ difference electron density map (Fig. 2). Structural perturbations of Cys-70, the H-bonded solvent network, and other features that are observed in the $F_L - F_A$ difference electron map are also very likely to occur during the fluorescence photocycle as part of the electrostatic response to chromophore ionization.

The electronic absorption spectrum of GFP_L (Fig. 3*B*) resembles that of recently identified ground state intermediates I_1 (500 nm) and I_2 (497 nm) in the fluorescence photocycle at room temperature (33), which relax to GFP_A with a 400-ps time constant, although the blue shift of the $I_1 \rightarrow I_2$ transition in the fluorescence pathway is smaller in magnitude than the blue shift occurring in the $GFP_L \rightarrow GFP_M$ transition in the phototransformation pathway. Complete relaxation to the GFP_R structure requires additional structural changes, including relaxation of Gln-69 (Fig. 3*A*), that are not likely to occur in the fluorescence cycle.

We propose that the very fast, low barrier structural changes reported here are functional in GFP, promoting optimal transformation through the fluorescence photocycle after the initial excited state ionization and inhibiting competing non-radiative processes. These fluid motions of the chromophore environment are unexpected, in light of its proposed role in suppressing the isomerization that quenches the fluorescence of the isolated chromophore (34). Apparently, picosecond timescale structural motions of water molecules and polar side chains in the chromophore environment stabilize the charge redistribution in the radiative state, accounting for the high fluorescence quantum efficiency under blue excitation. The low fluorescence quantum yields of the T203H (22) and T203H/Q69L mutants, where the interactions between the chromophore and the perturbed regions are diminished or removed, further support this proposal. In the T203H/Q69L mutant the chromophore may be partly shielded from solvent in the cavity, but importantly the H-bonding network connecting the chromophore with solvent, Gln-69, and Cys-70 will be disrupted. The spectroscopic properties of the double mutant do not indicate a character change of the electronic transitions, but show non-radiative decay channels to be strongly affected.

Even at low temperature, large changes in local structure of wild type GFP stabilize the charge redistribution following ionization of the buried chromophore. Indeed, excited state deprotonation remains operative at 77 K (at a reduced rate) and fluorescence emission occurs at 504 nm (3). This evidence further supports the existence of low barrier functional dynamics below the solvent glass transition (18). We note that, in the photoactive yellow protein, electrostatic rearrangements resulting from proton transfer between the buried Glu-46 and the chromophore phenolic oxygen ultimately cause the protein to partially unfold (35). This further underscores the dramatic electrostatic rearrangements that are also occurring during the fluorescence cycle of GFP. In GFP, we observe relatively strong difference electron density, in contrast to a number of other light-sensitive protein (15–17). Also, a recent study of the photosynthetic reaction center reported relatively strong difference electron density with illumination at low temperature (36). It should be pointed out that differences in data quality and data scaling cross-correlations hamper absolute comparison with other light-sensitive systems.

Proton transfer and charge redistribution are ubiquitous in biomolecular reactivity (37). The molecular mechanisms that stabilize the electrostatic changes in GFP, which are proposed to be linked to the surprisingly efficient suppression of non-radiative pathways, may therefore have wider ramifications. Structural dynamics are central in the description of quantum catalysis (37, 38) and Marcus electron transfer theory (39, 40). However, these dynamics are often not directly accessible and are generally determined indirectly from kinetic isotope effects or overall rate determinations, for example, in addition to computational approaches. GFP provides a well characterized model system that is suitable to quantify structural dynamics using ultrafast methods.

We expect that improved understanding of the GFP photocycle will facilitate re-engineering the protein to incorporate novel properties (1, 2) without sacrificing the desirable high fluorescence efficiency. In particular, the present results suggest that mutations in the neutral state background, which has the highest known fluorescence quantum efficiency, should retain the hydrogen bonding network, including Gln-69 and Cys-70 (Figs. 2 and 3).

Acknowledgments—We thank SRS personnel on beamline ID14-2 for assistance. We acknowledge use of the PIRATE facility at the Rutherford Appleton Laboratory, Chilton, UK (US/22/B/2/04 to J. V. T.) and thank Tony Parker for rapid access. The GFP crystals used in this work were prepared with the assistance of John Hamilton. We thank Keith Moffat for critical reading of the manuscript.

REFERENCES

1. Tsien, R. Y. (1998) *Annu. Rev. Biochem.* **67,** 509–544
2. Lippincott-Schwartz, J., Snapp, E., and Kenworthy, A. (2001) *Nat. Rev. Mol. Cell. Biol.* **2,** 444–456
3. Chattoraj, M., King, B. A., Bublitz, G. U., and Boxer, S. G. (1996) *Proc. Natl. Acad. Sci. U. S. A.* **93,** 8362–8367
4. Forster, T. (1950) *Zeitschrift für Elektrochemie und Angewandte Physikalische Chemie* **54,** 531–535
5. Weller, A. (1952) *Z. Elektrochem.* **56,** 662–668
6. Agmon, N. (2005) *J. Phys. Chem. A* **109,** 13–35
7. Brejc, K., Sixma, T. K., Kitts, P. A., Kain, S. R., Tsien, R. Y., Ormo, M., and Remington, S. J. (1997) *Proc. Natl. Acad. Sci. U. S. A.* **94,** 2306–2311
8. Palm, G. J., Zdanov, A., Gaitanaris, G. A., Stauber, R., Pavlakis, G. N., and Wlodawer, A. (1997) *Nat. Struct. Biol.* **4,** 361–365
9. Stoner-Ma, D., Jaye, A. A., Matousek, P., Towrie, M., Meech, S. R., and Tonge, P. J. (2005) *J. Am. Chem. Soc.* **127,** 2864–2865
10. Agmon, N. (2005) *Biophys. J.* **88,** 2452–2461
11. van Thor, J. J., Zanetti, G., Ronayne, K., and Towrie M. (2005) *J. Phys. Chem. B.* **109,** 16099–16108
12. van Thor, J. J., Gensch, T., Hellingwerf, K. J., and Johnson, L. N. (2002) *Nat. Struct. Biol.* **9,** 37–41
13. Yang, F., Moss, L. G., and Phillips, G. N., Jr. (1996) *Nat. Biotechnol.* **14,** 1246–1251
14. Vitkup, D., Ringe, D., Petsko, G. A., and Karplus, M. (2000) *Nat. Struct. Biol.* **7,** 34–38
15. Edman, K., Nollert, P., Royant, A., Belrhali, H., Pebay-Peyroula, E., Hajdu, J., Neutze, R., and Landau, E. M. (1999) *Nature* **401,** 822–826
16. Teng, T. Y., Srajer, V., and Moffat, K. (1994) *Nat. Struct. Biol.* **1,** 701–705
17. Schlichting, I., Berendzen, J., Phillips, G. N., Jr., and Sweet, R. M. (1994) *Nature* **371,** 808–812
18. Fenimore, P. W., Frauenfelder, H., McMahon, B. H., and Young, R. D. (2004) *Proc. Natl. Acad. Sci. U. S. A.* **101,** 14408–14413
19. Leslie, A. G. W. (1992) *Joint CCP4 + ESF-EAMCB Newsletter on Protein Crystallography*, No. 26, Warrington, United Kingdom
20. Collaborative Computational Project, Number 4 (1994) *Acta Crystallogr. Sect. D Biol. Crystallogr.* **50**, 760–763
21. Lamzin, V. S., Perrakis, A., Wilson, K.S. (2001) in *International Tables for Crystallography. Vol. F: Crystallography of Biological Macromolecules* (Rossmann, M. G., and Arnold, E., eds) pp. 720–722, Dordrecht, Kluwer Academic Publishers, The Netherlands
22. Lippincott-Schwartz, J., and Patterson, G. H. (2003) *Science* **300,** 87–91
23. Crameri, A., Whitehorn, E. A., Tate, E., and Stemmer, W. P. (1996) *Nat. Biotechnol.* **14,** 315–319
24. Towrie, M., Grills, D. C., Dyer, J., Weinstein, J. A., Matousek, P., Barton, R., Bailey, P. D., Subramaniam, N., Kwok, W. M., Ma, C., Phillips, D., Parker, A. W., and George, M. W. (2003) *Appl. Spectrosc.* **57,** 367–380
25. van Thor, J. J., Pierik, A. J., Nugteren-Roodzant, I., Xie, A., and Hellingwerf, K. J. (1998) *Biochemistry* **37,** 16915–16921
26. He, X., Bell, A. F., and Tonge, P. J. (2002) *Org. Lett.* **4,** 1523–1526
27. Barth, A. (2000) *Prog. Biophys. Mol. Biol.* **74,** 141–173
28. Delagrave, S., Hawtin, R. E., Silva, C. M., Yang, M. M., and Youvan, D. C. (1995) *Biotechnology* (*N. Y.*) **13,** 151–154
29. Chu, K., Vojtchovsky, J., McMahon, B. H., Sweet, R. M., Berendzen, J., and Schlichting, I. (2000) *Nature* **403,** 921–923
30. Kriminski, S., Kazmierczak, M., and Thorne, R. E. (2003) *Acta Crystallogr. Sect. D Biol. Crystallogr.* **59,** 697–708
31. Ormo, M., Cubitt, A. B., Kallio, K., Gross, L. A., Tsien, R. Y., and Remington, S. J. (1996) *Science* **273,** 1392–1395
32. Nie, B., Stutzman, J., and Xie, A. (2005) *Biophys. J.* **88,** 2833–2847
33. Kennis, J. T., Larsen, D. S., van Stokkum, I. H., Vengris, M., van Thor, J. J., and van Grondelle, R. (2004) *Proc. Natl. Acad. Sci. U. S. A.* **101,** 17988–17993
34. Niwa, H., Inouye, S., Hirano, T., Matsuno, T., Kojima, S., Kubota, M., Ohashi, M., and Tsuji, F. I. (1996) *Proc. Natl. Acad. Sci. U. S. A.* **93,** 13617–13622
35. Xie, A., Kelemen, L., Hendriks, J., White, B. J., Hellingwerf, K. J., and Hoff, W. D. (2001) *Biochemistry* **40,** 1510–1517
36. Baxter, R. H., Seagle, B. L., Ponomarenko, N., and Norris, J. R. (2004) *J. Am. Chem. Soc.* **126,** 16728–16729
37. Benkovic, S. J., and Hammes-Schiffer, S. (2003) *Science* **301,** 1196–1202
38. Sutcliffe, M. J., and Scrutton, N. S. (2002) *Eur. J. Biochem.* **269,** 3096–3102
39. Moser, C. C., Keske, J. M., Warncke, K., Farid, R. S., and Dutton, P. L. (1992) *Nature* **355,** 796–802
40. Page, C. C., Moser, C. C., Chen, X., and Dutton, P. L. (1999) *Nature* **402,** 47–52